Rational Molecular Design Enables Efficient Blue TADF–OLEDs with Flexible Graphene Substrate

Parisa Sharif‡, Eda Alemdar‡, Soner Ozturk, Omer Caylan, Tugba Haciefendioglu, Goknur Buke, Murat Aydemir, Andrew Danos, Andrew P. Monkman, Erol Yildirim, Gorkem Gunbas, Ali Cirpan* Ahmet Oral**

‡ These authors contributed equally.

Dr. P. Sharif, Dr. E. Yildirim, Prof. G. Gunbas, Prof. A. Cirpan, Prof. A. Oral
Micro and Nanotechnology Graduate Program
Middle East Technical University
Ankara 06800, Turkey
e-mail: ggunbas@metu.edu.tr, acirpan@metu.edu.tr, orahmet@metu.edu.tr

E Alemdar, T. Haciefendioglu, Dr. E. Yildirim, Prof. G. Gunbas, Prof. A. Cirpan
Department of Chemistry
Middle East Technical University
Ankara 06800, Turkey

S. Ozturk
TENMAK Boron Research Institute
Ankara 06800, Turkey

O. Ceylan, Dr. G. Buke
Micro and Nanotechnology Grad. Program
TOBB University of Economics and Technology
Ankara 06560, Turkey

Dr. G. Buke
Department of Materials Science and Nanotechnology Engineering
TOBB University of Economics and Technology
Ankara 06560, Turkey

Dr. M. Aydemir
Department of Fundamental Sciences
Erzurum Technical University
Erzurum, Turkey

Dr. A. Danos, Prof. A.P. Monkman
Department of Physics,
Durham University, Lower Mountjoy, Stockton Road, Durham, DH1 3LE UK

Dr. E. Yildirim, Prof. G. Gunbas, Prof. A. Cirpan
Polymer Science and Technology Graduate Program
Middle East Technical University
Ankara 06800, Turkey

Dr. P. Sharif, Prof. G. Gunbas, Prof. A. Cirpan, Prof. A. Oral
METU GUNAM Center
Middle East Technical University
Ankara 06800, Turkey

Keywords: OLED, TADF, graphene, flexible OLED, blue OLED, 2D material, graphene anode, heavy atom effect

Abstract

Observation of thermally activated delayed fluorescence (TADF) in conjugated systems redefined the molecular design approach to realize highly efficient organic light emitting diodes (OLEDs) in the early 2010s. Enabling effective reverse intersystem crossing (RISC) by minimizing the difference between singlet and triplet excited state energies (ΔE_{ST}) has proven to be a widely applicable and fruitful approach, which resulted remarkable external quantum efficiencies (EQE). The efficacy of RISC in these systems is mainly dictated by the first-order mixing coefficient (λ), which is proportional to spin-orbit coupling (H_{SO}) and inversely proportional to ΔE_{ST}. While minimizing ΔE_{ST} has been the focus of the OLED community over the last decade, the effect of H_{SO} in these systems has been largely overlooked. Here, we designed and synthesized molecular systems with increased H_{SO} by substituting select heteroatoms of high-performance TADF materials with heavy-atom selenium. A new series of multicolour TADF materials (Se-TADFs) with remarkable EQEs were achieved. One of these materials, **SeDF-B**, resulted in pure blue emission with EQEs approaching 20%.

Additionally, flexible graphene-based electrodes were developed for OLEDs and revealed to have similar performance as standard indium tin oxide (ITO) in most cases, while remarkably

surpassing ITO/Glass in pure blue OLED devices. These devices are the first report of TADF based OLEDs that utilize graphene-based anodes.

1. Introduction

Organic conjugated molecules are promising candidates to replace their inorganic counterparts in color display technologies due to their ease of processability, low cost, flexibility, pure color emission, low operational voltages, and high efficiency.[1] The optoelectronic performance of highly efficient OLEDs is dependent on effective utilization of electrical generated non-emissive triplet excitons. There are two main approaches to achieve this; phosphorescent materials with heavy metals such as Ir and Pt improve H_{SO} to allow direct triplet emission, while thermally active delayed fluorescence (TADF) enabled by effective RISC converts triplets back into emissive singlet excitons.[2] Appropriate heavy metals for utilization in efficient OLEDs possess several disadvantages though – they are rare are expensive, potential pollutants, and blue emitters have short operational lifetimes due to their weak metal-ligand bonds – which together hinder their wide industrial utilization and stimulated the development of TADF materials.[3]

In TADF efficacy of RISC is mainly dictated by the first-order mixing coefficient (λ), which is proportional to spin-orbit coupling (H_{SO}) and inversely proportional to ΔE_{ST}. By significantly reducing the gap between singlet and triplet excited state energies (ΔE_{ST}) – via spatially separating donor (D) and acceptor (A) units and creating almost orthogonal and localized HOMO and LUMO orbitals– OLEDs with records external quantum efficiencies have been achieved. Surprisingly, the effect of the other key player in the equation, H_{SO}, has been largely overlooked by the community as it is not as straightforward to investigate or engineer as the types of D and A subunits and their connectivity.[4–14]

Alongside high efficiencies, one of the unique abilities of OLEDs compared to other lighting sources is the possibility of creating flexible devices; hence, alternative flexible anodes and

substrates have attracted significant attention from OLED community in recent years. [15,16] ITO is the most common transparent anode for conventional OLEDs due to its superior optical and electrical properties. However, ITO on polymer substrates is not an ideal electrode due to brittleness and the scarcity and cost of indium. Graphene (Gr)—a flexible, transparent, 2D sheet of sp^2-hybridized abundant carbon atoms— has meanwhile evolved into a promising alternative as an electrode material due to its remarkable electrical, mechanical, and optical properties.[17–19] However, its low work function (WF, 4.4 eV) and high sheet resistance (300 Ω/sqr) limit its use in practical optoelectronic applications.[20] The low WF of Gr causes a significant injection barrier with overlaying organic emitters and transport layers. The high sheet resistance of pristine Gr results in high turning-on voltages, thus reducing luminous efficiencies in OLEDs. Various approaches have been reported to overcome these disadvantages of Gr for OLED applications with appreciable success.[20–25] However, a true ITO alternative for efficient OLEDs is yet to be achieved.

In this paper, we designed and synthesized a new family of TADF emitters with selenium incorporated into the D unit, orthogonally coupled to a series of A units, to increase H_{SO} and minimize DE_{ST} simultaneously. The approach provided enhanced EQEs compared to similar TADF emitters with no heavy-atom utilization. Remarkably one of the derivatives resulted in pure blue emission with EQEs approaching 20%.

Additionally, by carefully optimizing the growth, surface modification, and doping processes, Gr-based flexible anodes revealed similar performance to ITO/glass substrates. In pure blue OLED devices utilizing our TADF emitter **SeDF-B**, Gr/PET anodes developed in this work outperformed ITO/Glass electrodes. These Gr-based devices are the first-ever utilization of Gr anodes for TADF OLEDs.

2. Molecular Design, Computational Studies, and Synthesis

Our design principle was that increasing H_{SO} while simultaneously maintaining ΔE_{ST} should enhance λ and thus accelerate RISC rate. Hence, we carefully selected high-performance phenoxazine-based TADF materials already reported in the literature and substituted the oxygen atoms in D units with the selenium atom, which possesses significantly higher H_{SO} than oxygen (Figure 1).[26] The possibility of utilizing large chalcogens was omitted since it was shown that long-term accumulation of the corresponding anions of the aforementioned chalcogens at metal interfaces is detrimental to OLED performance.[27] The literature emphasizes that the effects of heavy chalcogens in OLEDs are still not fully understood due to the lack of device-centered studies.[28,29] In 2019, Monkman et al. synthesized a D-A-D type TADF molecule using the same donor group used in this study and replaced the sulfur in the donor unit of the molecule with selenium,[30,31] causing dual emission. [5] In the above-mentioned study, it was observed that there was not much heavy atom effect on TADF as the Se atom allowed for more significant structural changes that opened up the CT emission from a different ax/eq conformer. However, using selenium atom in this study significantly improved the TADF properties, and the heavy atom effect was revealed.

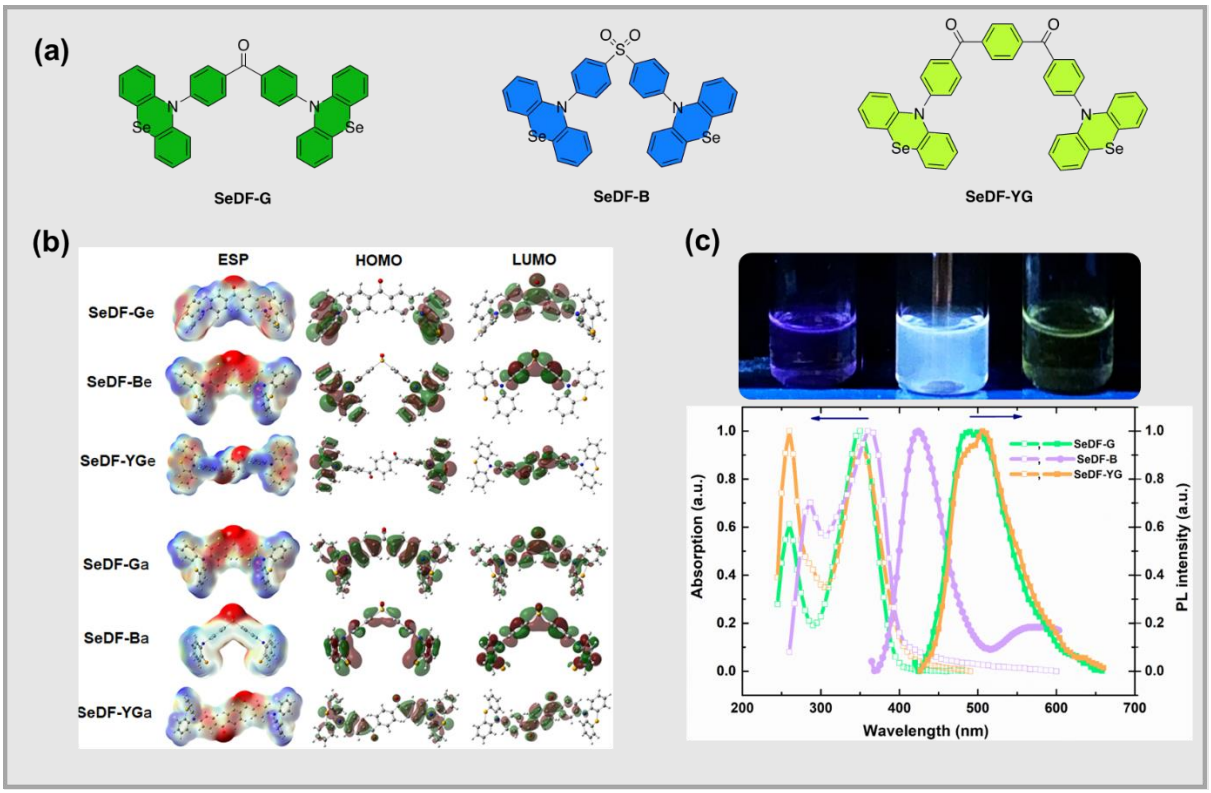

Figure 1 a) Structures of TADF materials of SeDF-G, SeDF-B, and SeDF-YG. b) Electrostatic potential surface (ESP) and frontier molecular orbital surfaces (HOMO, and LUMO) for the SeDF-G, SeDF-B, and SeDF-YG TADF materials in the equatorial (upper) and axial (lower) conformation of the donor, c) Luminescence images of SeDF-G, SeDF-B, and SeDF-YG in chloroform recorded under UV irradiation at λ_{ex}=365 nm (above), normalized absorption (dashed line) and photoluminescence (PL, solid line) spectra of SeDF-G, SeDF-B and SeDF-YG in chloroform at room temperature (below).

The lowest energy structures calculated for the designed TADF materials presented two different conformations that are either planar or orthogonal, corresponding to quasi-axial (*a*) and quasi-equatorial (*e*) conformers, respectively (Supplementary Fig. S1-2). Although the quasi-axial conformers exhibit lower energy than quasi-equatorial conformers with ~0.1-0.2 eV energy difference, previous studies demonstrated that both structures were observed experimentally.[32–35] This indicates TADF materials with selenium substituted phenoxazine (Se-PXZ) derivatives may have dual conformations due to the difference in the C-N and C-Se

bond lengths in the D group as previously reported for PXZ and PTZ difference. The nearly orthogonal equatorial conformers resulted in the lower energy excited states having a smaller ΔE_{ST}, while axial conformers possess higher singlet state energy level with stronger oscillator frequency and more classical fluorescence characteristics. Also, axial conformations have deeper HOMO and higher LUMO levels than the other two structures, resulting in higher energy S_0-S_1 and S_1-T_1 transitions. Equatorial instead conformations have lower S_0-S_1 and S_1-T_1 (ΔE_{ST}) transition energies, beneficial to the TADF materials. Lower ΔE_{ST} was calculated for SeDF-Be compared to SeDF-Ba since the singlet-triplet gap grows with increasing overlap of the frontier orbitals (Table 1). The axial conformations have extended π-delocalization with strong HOMO-LUMO overlap due to electron delocalization. Highly localized HOMO and LUMO orbitals and high charge density difference between D and A were instead observed for the equatorial conformers as desired for TADF materials (Figure 1b).

Table 1 Results for the DFT calculations for the electronic and structural properties of SeDF-G-3 and the effect of phenoxazine and phenothiazine substitutions. All energies are in eV, dipole and polarizability calculations are in Debye and a.u, respectively. Calculations based on the PBE0 functional are given in parenthesis.

	HOMO	**LUMO**	**ΔE_{S0-S1}**	**ΔE_{S0-T1}**	**ΔE_{T1-S1}**	**ΔE_{T2-S1}**	**ΔE_{T2-S2}**	**ΔE_{T1-T2}**
SeDF-Ga	-5.64 (-5.85)	-1.53 (-1.35)	3.33 (3.31)	2.85 (2.85)	0.48 (0.46)	0.33 (0.30)	0.56 (0.69)	0.15 (0.16)
SeDF-Be	-5.54 (-5.74)	-2.21 (-2.10)	2.79 (2.93)	2.76 (2.87)	0.03 (0.06)	-0.27 (-0.12)	0.31 (0.47)	0.30 (0.13)
SeDF-Ba	-5.73 (-5.94)	-1.30 (-1.14)	3.47 (3.38)	3.20 (3.15)	0.27 (0.23)	0.13 (0.10)	0.46 (0.65)	0.14 (0.13)
SDF-Be	-5.53 (-5.94)	-2.25 (-2.13)	2.73 (2.89)	2.71 (2.84)	0.02 (0.04)	-0.27 (-0.10)	0.31 (0.50)	0.30 (0.50)

SDF-Ba	-5.74 (-5.98)	-1.30 (-1.14)	3.47 (3.38)	3.19 (3.15)	0.28 (0.24)	0.14 (0.11)	0.47 (0.65)	0.14 (0.13)
ODF-Be	-5.33 (-6.31)	-2.30 (-2.15)	2.46 (2.46)	2.45 (2.62)	0.01 (0.02)	-0.37 (-0.19)	0.23 (0.43)	0.38 (0.21)
SeDF-YG	-5.82 (-6.03)	-2.09 (-1.93)	3.01 (3.02)	2.45 (2.62)	0.29 (0.28)	0.26 (0.23)	0.56 (0.69)	0.03 (0.04)
	μ	**α**	**β**	**λ_{hole}**	**AIP**	**VIP**	**VEA**	**$\delta_{acceptor}$**
SeDF-G	4.14	538.00	2519.67	0.13	6.60	6.67	-0.44	0.44
SeDF-Be	3.29	527.52	111.80	0.39	6.35	6.54	-1.00	0.93
SeDF-Ba	6.92	528.21	1136.02	0.15	6.68	6.76	-0.36	0.27
SDF-Ba	6.72	514.47	1362.42	0.16	6.68	6.78	-0.36	0.24
SDF-Be	2.98	513.78	25.33	0.41	6.33	6.53	-1.03	0.76
ODF-Be	2.80	483.46	24.95	0.17	6.24	6.34	-1.05	0.07
SeDF-YG	0.00	643.96	1.00	0.13	6.65	6.71	-0.95	0.39

As a result of theoretical calculations, we determined two main differences provided by the heavy ion effect by using phenoxazine (PXZ), phenothiazine (S-PXZ or PTZ) and phenoselenazine (Se-PXZ or PSeZ) derivatives for the blue OLED TADF material. First one is structural difference where as it was also previously reported that while phenoxazine prefer to have equatorial conformation, phenothiazine and phenoselenazine derivatives have dual conformations leading to the dual emission due to the energy transfer between conformations (Supplementary Fig. S1-S2).[32,36,37] In addition to the axial and equatorial difference, sulfur and selenium atoms prefer to position out of aromatic plane significantly compared to the planar phenoxazine (Supplementary Fig. S3) that increases number of possible conformations with energy difference as low as thermal energy of the room temperature given as two different axial conformations in Supplementary Fig. S1.

The second contribution provided by the heavy atom effect is sourced from electronic effects. The percentage of HOMO on the acceptor center increases, while percentage of the LUMO on the acceptor decreases with the heavy atom effect (Supplementary Table S2). Dipole moment,

polarizability and hyperpolarizability is increasing generally in the order of O, S, Se. Positive atomic charges based on the electrostatic potential fitting is increased on the acceptor center and negative charge on the donor that means stronger electron density donating potential by sulfur and selenium substitution. The most significant enhancement is improvement in theoretically calculated k_{RISC} especially for the equatorial conformation of the phenothiazine and phenoselenazine substituted TADF materials determined for different λ_M values for $T_1 \rightarrow S_1$ transition. The origin of this enhancement is determined mainly as the enhancement of H_{SO}, spin orbit coupling matrix element, that show more than tenfold increase by the replacement of O with Se atom.[38] Our results presented that structures only with equatorial conformations show significant improvement for k_{RISC} leading to the TADF properties (Table 2). k_{RISC} is significantly lower for the more stable axial conformations. This indicates multi-conformational structure by heavy atom substitution leading to the classical fluorescence by axial conformations and TADF type emission by equatorial conformations that enhance EQE. Although percentage of the equatorial conformation responsible for the TADF properties decreases by PSeZ substitution, the efficiency is much higher due to the tremendous enhancement in the spin orbit coupling and dual emission by energy transfer between conformations.

Table 2. k_{RISC} for $T_1 \rightarrow S_1$ transitions and the $\Delta E_{S1\text{-}T1}$ and H_{SO} parameters used for the calculation of k_{RISC}.

	$\Delta E_{S1\text{-}T1}$ (eV)	H_{SO} (cm^{-1})	k_{RISC} (λ_M=0.1 eV)	k_{RISC} (λ_M=0.2 eV)
O-DF-Be	0.01	9.2	2.13E+10	5.72E+09
S-DF-Be	0.02	21.4	9.22E+10	2.51E+10
S-DF-Ba	0.28	3.1	6.21E+03	7.52E+04
Se-DF-Be	0.03	90	2.35E+12	6.56E+11
Se-DF-Ba	0.27	3.6	1.74E+04	1.61E+05
Se-DF-Ge	0.01	110	4.42E+12	1.21E+12
Se-DF-Ga	0.48	4.1	8.35E-05	1.65E+00
Se-DF-YGe	0.02	52	1.10E+12	3.00E+11

Se-DF-YG*a*	0.29	2.9	2.57E+03	4.11E+04

According to theoretical calculations, all three materials would possess dual conformations including a quasi-axial conformer with classical fluorescence emission behavior and a quasi-equatorial conformer with TADF characteristics that was further supported by the natural transition orbitals (Supplementary Fig. S4) for the first singlet and triplet excitations. Improved planarity of the donor unit was observed for these excitations (Supplementary Fig. S5). Among equatorial conformers, SeDF-Ge exhibits higher molar absorptivity (Supplementary Fig. S6). [32,33]

We concluded that similar to the previous studies conducted for PTZ, [34–36] having a nonplanar six-membered phenothiazine ring leading to a high EQE due to the presence of sulfur atom; efficient OLED materials can also be designed by selenium substitution in PTZ to utilize control of dual conformations. Dual emission and energy transfer between these two conformations could combine due to the structural and electronic heavy atom effect by the selenium atom leading to enhanced performance in TADF-OLED materials. [39]

With our main design principle supported by encouraging computational results, we set out to synthesize these interesting targets. The synthetic pathway for the target molecules is given in Scheme 1. The synthesis started with diphenylamine, and selenium incorporation was performed using SeO_2 and I_2 to get the target donor unit (**1**) in moderate yield. [40] Acceptor unit **2** was synthesized from commercially available terephthaloyl chloride and bromobenzene using Friedel-Crafts chemistry. Compounds SeDF-G and SeDF-YG were realized by Buchwald-Hartwig coupling in good yields. Finally, SeDF-B was synthesized using commercial bis-(4-fluorophenyl)sulfone and donor **1** using NaH in DMF.

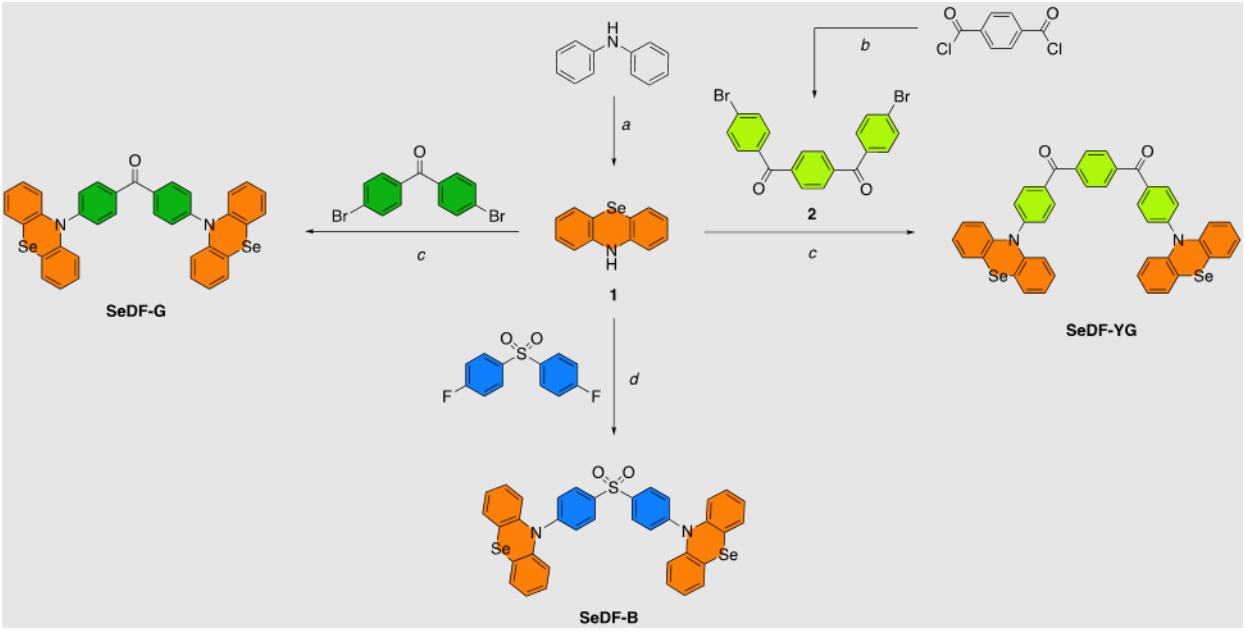

Scheme 1 Synthetic pathways for the TADF materials (SeDF-G, SeDF-YG, SeDF-B): Reagents and Conditions: (*a*) SeO2, I2, 180 ºC, 48%; (*b*) bromobenzene, AlCl3, rt → 90 ºC; (*c*) Pd2(dba)3, (t-Bu)3P, NaO-tBu, Toluene, 125 ºC, 82%; (*d*) NaH, DMF, 60 ºC, 28%.

2.1 Photophysical Properties

Ultraviolet-visible (UV-Vis) absorption and photoluminescence (PL) spectra of SeDF-G, SeDF-B, and SeDF-YG are given in chloroform solution (Figure 1c), with different emission bands due to the different acceptor strengths of the different acceptors. Figure 2 shows the PL and phosphorescence (PH) spectra of the molecules in drop-cast films at room temperature (RT) and 80K (10% w/w loading in mCBP host), respectively. The blueshifted PH spectra for all three materials are nearly identical, and so most likely arise from the common D unit. The PL spectra occurs at longer wavelengths than time-resolved PH (80K, 80ms delay) in the films, so we attribute the PH to a higher LE triplet state while the PL comes from a lower energy charge transfer (CT) state. Se-B has a weaker A unit, which results in blueshifted emission (E_S=2.84 eV), but Se-G and Se-YG have approximately comparable E_S values (E_S=2.71 eV). From the onsets of the PL and PH spectra, ΔE_{ST} is smaller for Se-B (E_{ST}=0.08 eV) and larger for Se-G and Se-YG molecules (E_{ST}=0.15eV).

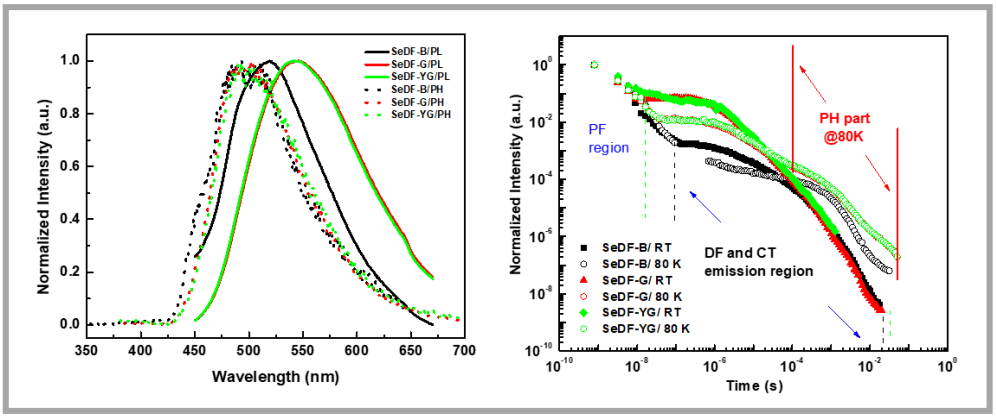

Figure 2. Left: Normalized photoluminescence spectra of **Se-B, Se-G and Se-YG** molecules in 10% mCBP drop-cast films at RT. Phosphorescence spectra were taken at 80 K at >80ms delay after pulsed excitation. Right: Photoluminescence decay kinetics of the same films at RT (under vacuum) and at 80K (under dry nitrogen).

The time-resolved emission spectra and intensity decays for the films were recorded as previously described[41] and are shown in Figure 2b, with representative individual spectra (and contours of the normalized time-resolved spectra) shown in Figure 3. Similar spectra and decays at 80K are shown in Figure S19, revealing the phosphorescence spectrum, with significantly suppressed delayed fluorescence observed at lower temperatures. The decays were also fit entirely using a kinetic model,[42] as well as with double exponentials across the separate prompt fluorescence (PF) and delayed fluorescence (DF) time regimes, with fitting parameters given in Table 3.

Similar to the steady-state spectra in Figure 1, the time-resolved spectra and decays reveal similar TADF performance for **Se-G** and **Se-YG** (with strongly analogous acceptor units), but significantly different behavior in **Se-GB**. In **Se-GB** the PF spectra are in the near-UV region (~350nm), corresponding to strong LE emission from the D unit. This UV emission decays rapidly, eventually being replaced with strongly redshifted CT emission (~500nm). The rapid

decay of the D emission contributes to the much larger value of k_f in the fitted decays of the blue emitter, as well as the seemingly lower DF contribution in the normalized decay (Figure 2). The same D emission is also observed in the PF of the other two materials, but to a significantly lower extent. Instead for these materials the LE and CT emission occur simultaneously at first, with the CT emission dominating throughout. At intermediate times we also observe an additional CT emission peak at ~425nm. We suggest that this arises from the higher energy axial conformer in the as-deposited films. This emission is short-lived though, as both energy transfer to nearby axial conformers as well as geometry relaxation in individual molecules will quench this emission band while transferring energy to the equatorial band.

Amongst the other decay parameters, the intersystem crossing rates (k_{ISC}) are noted to be rather high in all three materials. In **Se-G** and **Se-YG** this is likely due to the impact of the heteroatom ketone, which is able to generate triplet states efficiently, leading to large DF contributions. Although the ISC is also fast in **Se-B** -possibly due to spin conversion as charges separate from the PF-emissive LE state to form the CT state responsible for DF emission - its lower rate of RISC leads to a lower overall DF contribution. This slower RISC in **Se-B**, despite its smaller ΔE_{ST}, further demonstrates that this energy gap is not the sole determining factor in predicting TADF performance. [43,44]

Table 3: Decay parameters k_f, k_{ISC}, k_{rISC} and lifetimes from kinetic fitting of decays

	k_f ($x\ 10^7\ s^{-1}$)	k_{ISC} ($x\ 10^7\ s^{-1}$)	k_{rISC} ($x\ 10^6\ s^{-1}$)	τ_{prompt} (ns) [a]	$\tau_{delayed}$ (µs) [a]
SeDF-B	1.98	9.88	0.59	τ_1=2.47 τ_2=8.6 τ_{ave}=3.0	τ_1=6.45 τ_2=133 τ_{ave}=18.5
SeDF-G	0.49	9.22	5.69	τ_1=1.44 τ_2=18.8 τ_{ave}=1.5	τ_1=3.1 τ_2=90 τ_{ave}=3.9
SeDF-YG	0.27	9.7	10.6	τ_1=6.46 τ_2=38.7 τ_{ave}=9.7	τ_1=3.6 τ_2=95 τ_{ave}=4.6

[a] Lifetimes, and their weighted averages from double exponential fitting of either PF or DF regions.

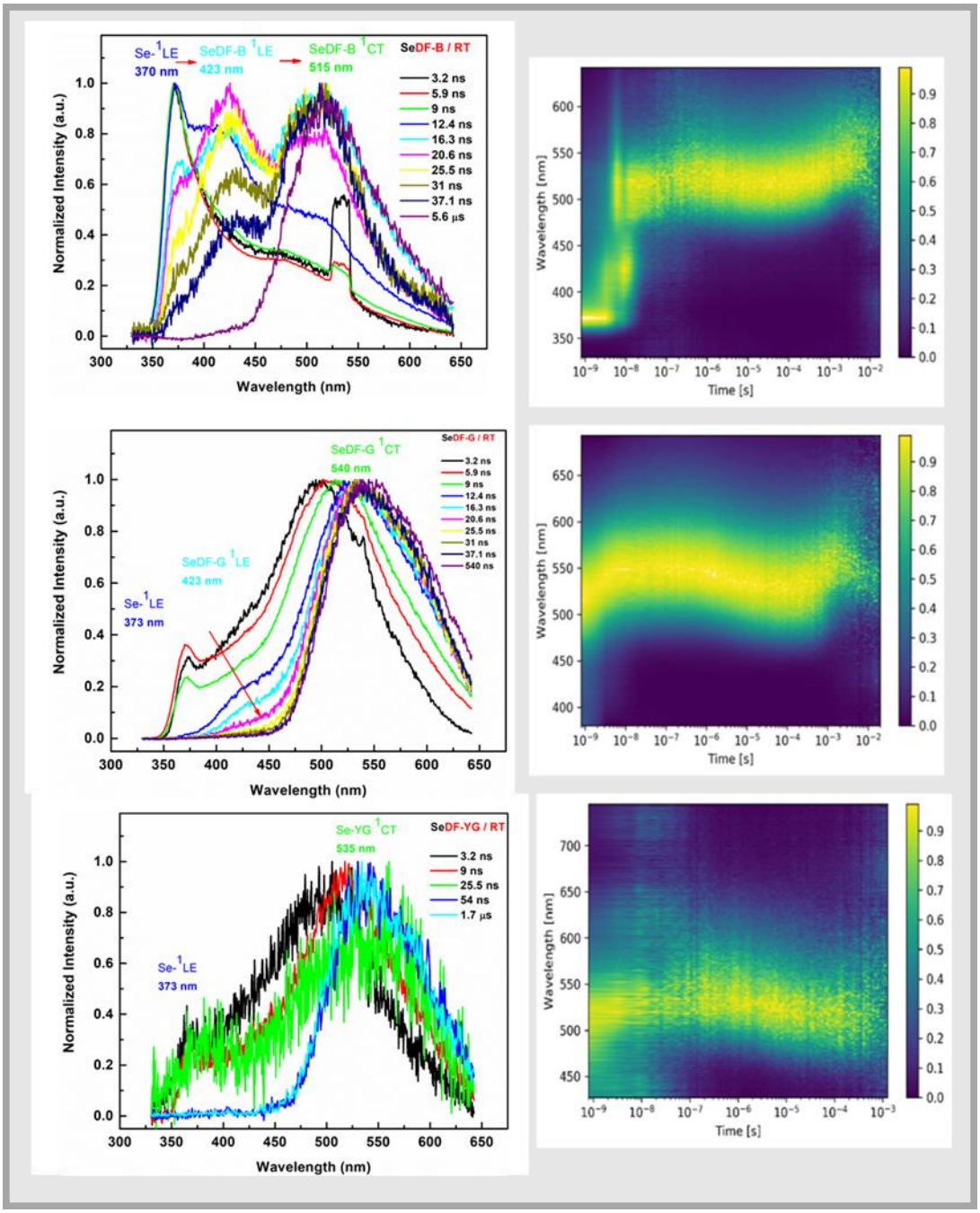

Figure 3. Normalized time-resolved spectra at RT (left), with. contour plots of normalised time-resolved spectra (right). The emission spectra change from Se-^{1}LE- dominated at early times, to redshifted CT-dominated emission at later times

3. Graphene Growth

Chemical Vapor Deposition (CVD) is the most common technique used to synthesize single-layer graphene (SLG) films. Various optimization studies on different gas ratios and growth temperatures have been performed to grow high-quality SLG films on various substrates.[45–48] However, the key requirement is to grow SLG films with low sheet resistance and high mobility for next-generation OLED applications. In this work, a 25 µm-thick cold-rolled copper foil was used as a growth substrate to achieve highly uniform large are Gr films. Pre-cleaning of copper using acid treatment is also crucial, which significantly improves both uniformity and morphology by lifting the oxide layer and removing the existing impurities on the copper foil.[49] Although superior in terms of quality and uniformity, SLG has a low intrinsic charge concentration compared to multi-layer graphene (MLG), resulting in high sheet resistance (R_s). Therefore, we first optimized the SLG growth and then formed a multi-layer structure on PET substrates by repetitive transfer of optimized SLG and etching of the Cu sheets. The process of graphene synthesized is shown in Fig. S7. The layer number of synthesized Gr films was confirmed by Raman spectroscopy. The sharp 2D peak in the Raman spectrum verifies the single layer nature of the Gr film consistent with the literature (see Fig. 4a).[50]

The Raman results were also complemented with optical transmittance measurements. Gr films were transferred onto poly(ethylene tetraphthalate) (PET) films to prepare MLG samples with 1 and 7 layers of Gr, and the optical transmittance was measured (Figure 4a). Our results are consistent with the literature, where a ~2.3 % drop in transmittance was observed per Gr layer at 550 nm. The morphology of Gr was analyzed by scanning electron microscopy (SEM). SEM image (Figure 4b) revealed no impurities or major defects on the surface of the graphene-copper film (Fig. S8). To further analyze the continuity of the synthesized graphene, oxidation studies were performed. The areas where Gr was grown will be protected the underlying copper from oxidation, while the discontinuous regions will turn into dark orange due to oxidation. The

optical image of the oxidized copper foil is given in Fig 4b inset, proving that highly continuous Gr films were achieved.

The main drawback of graphene films compared to the ITO is their high sheet resistance. Several different dopants have been used to enhance the electrical properties of pristine Gr on rigid substrates.[20,21,23,24] Doping materials can be classified into two main groups: (1) inorganic acids (most commonly HNO_3, HCl, H_2SO_4), and (2) transition metal halides (most commonly $AuCl_3$, $FeCl_3$), where both utilize charge transfer processes on the Gr surface (shift in Fermi level) towards enhancement of conductivity, thus lowering sheet resistance (Figure 4b).

In this work, inspired by the doping studies for graphene on quartz substrates in literature,[51] two different approaches (inter-layer and last-layer doping) were optimized to reduce the high sheet resistance of MLG films on PET. In the first approach, doping is performed for each layer separately, while in the second approach the Gr film is doped after the whole multi-layer stack is already formed on the PET (see Figure 4c). Last-layer doping showed significantly better results, where MLG films with sheet resistance as low as 29.3 Ω/sqr were achieved.

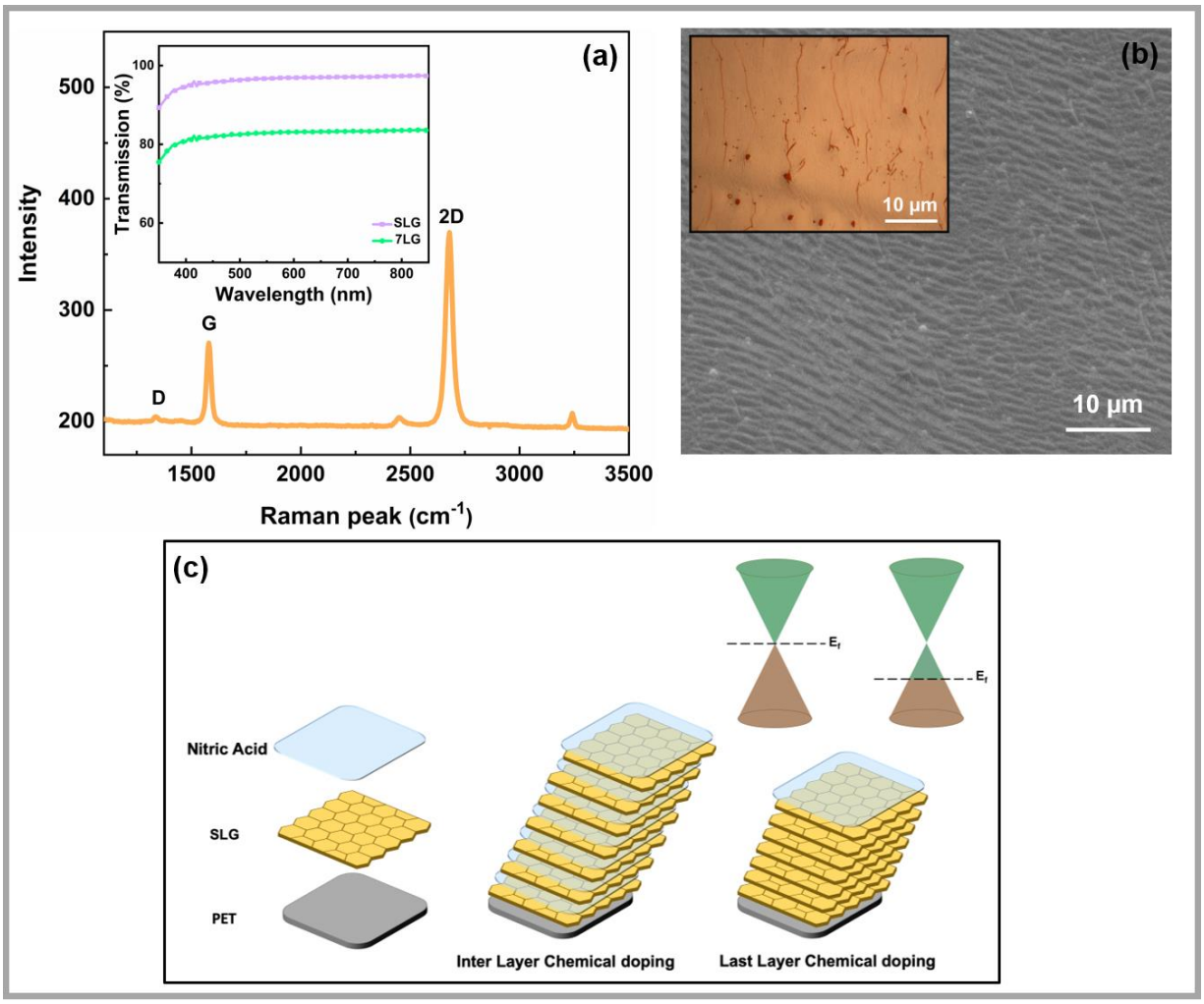

Figure 4. Characterization of single-layer graphene. a) Raman spectrum of single-layer graphene. Inset: Optical transmission spectra of SLG and 7LG. b) SEM image of single-layer graphene. Inset: Optical image of single-layer graphene after attempted oxidation of copper substrate. c) Inter-layer, and last-layer chemical doping methods. Inset: Effect of chemical doping on the band gap of graphene films.

4. Device Fabrication and Characterization

To investigate the potential of graphene/PET anodes and having confirmed the TADF activity of the new selenium-substituted emitters, OLEDs were fabricated utilizing both Gr- and ITO-based anodes. The device architectures and the energy level diagrams are given in Figure 5.

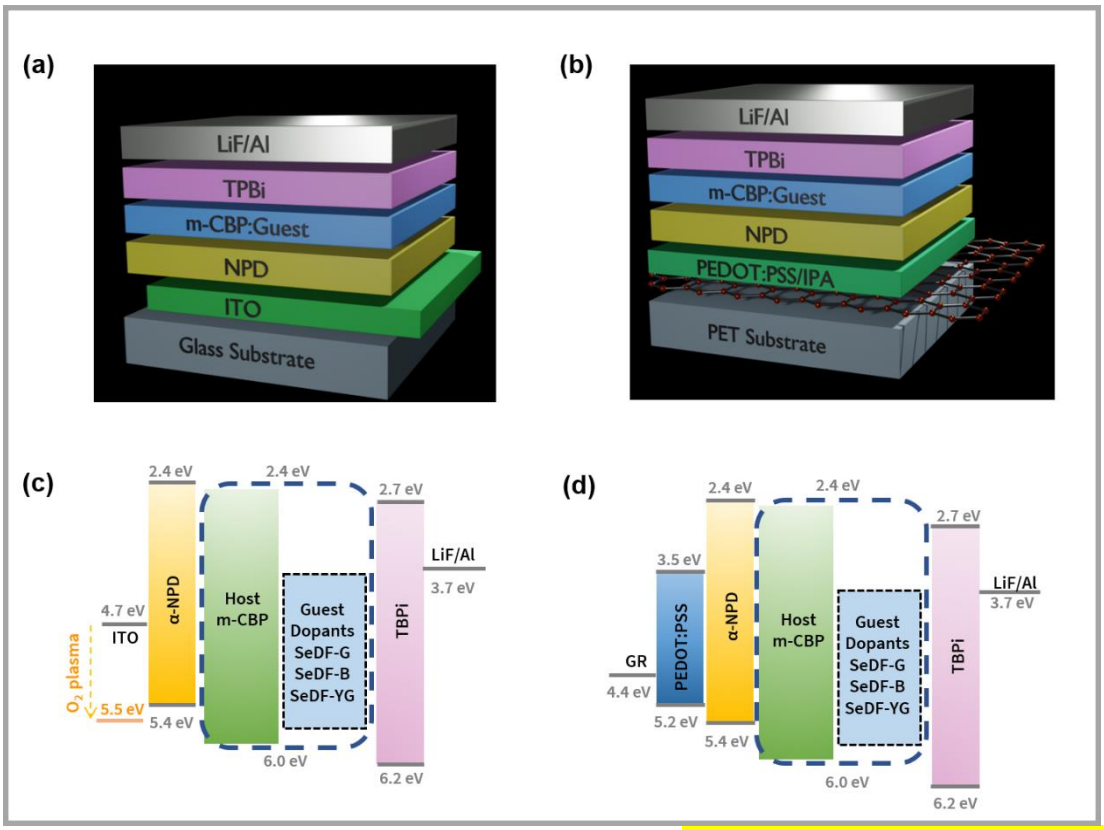

Figure 5. Device architectures of (a) ITO-based and (b) Gr-based devices and energy band alignments of (c) ITO-based devices and (d) Gr-based devices.)

As the Gr WF is lower than ITO, a hole injection layer (HIL) is necessary for band alignment between the anode and hole transport layer (HTL, here) (α-NPD) to ensure good charge injection and charge transport properties, which are crucial for achieving high efficiency OLEDs.[52] Several methods have been reported for modifying the Gr anode WF, such as treatment with oxygen plasma, ultraviolet-ozone, and insertion of an ultra-thin buffer layer (MoO_3, WO_3, PEDOT: PSS and PFSA).[52] PEDOT:PSS was chosen as the HIL layer since it has been well studied and shown to enhance the efficiency and lifetime of Gr-based OLEDs.[21,52]

To prevent the well-known wettability issue between Gr and PEDOT:PSS,[53] isopropyl alcohol (IPA) diluted PEDOT:PSS suspension was chosen as the HIL precursor. The PEDOT:PSS/IPA ratio was optimized via fabrication and characterization of OLEDs (PET/Gr/PEDOT:PSS/m-**CBP:SeDF-G**/TBPi/LiF/Al) with different proportions. **SeDF-G** was chosen as the emissive layer dopant for optimization studies due to its ease of synthesis and higher yields. Our initial

devices with the structure mentioned above gave either extremely low light output (best results obtained with 1:2 ratio) or devices that degraded before any light emission. At this point, we attributed this poor performance to possible charge imbalance and shift of recombination zone (RZ) to the anode side. To address this problem, electron transport layer (ETL) thickness optimizations were performed to improve the charge balance and RZ confinement.[54] A significant improvement was observed with this approach – from barely working devices to devices with EQEs over 20%, as detailed below – and the optimum thickness for ETL was determined to be 80 nm for Gr-based OLEDs. The RZ expanded towards the cathode side as the thickness increased, causing redshift observed in the electroluminescence (EL) spectra (Supplementary Fig. S9).

The performances of the fully optimized devices (Figure 6) prove that by mitigating the shortcomings of Gr anodes with appropriate doping and HIL, it is possible to match the EQE values of ITO-based non-flexible devices.[55] Once we obtained competitive results, we re-optimized our HIL layer to achieve the results in Figure 6. This time, the optimum PEDOT:PSS/IPA ratio was determined to be 1:1.5 for Gr-based devices. There was no need to introduce HILs for the ITO-based devices since it has been shown in the literature that increased O_2 plasma durations (~15 minutes) increase the work function of the ITO to desired levels.[56,57] It is also known that O_2 plasma treatment can modify the work function of Gr; however, longer plasma treatment durations result in unpredictable detachment of the graphene layers. Hence a short O_2 plasma treatment (~5 minutes) to remove organic contaminants was performed on the Gr-coated PET substrates before PEDOT:PSS deposition.

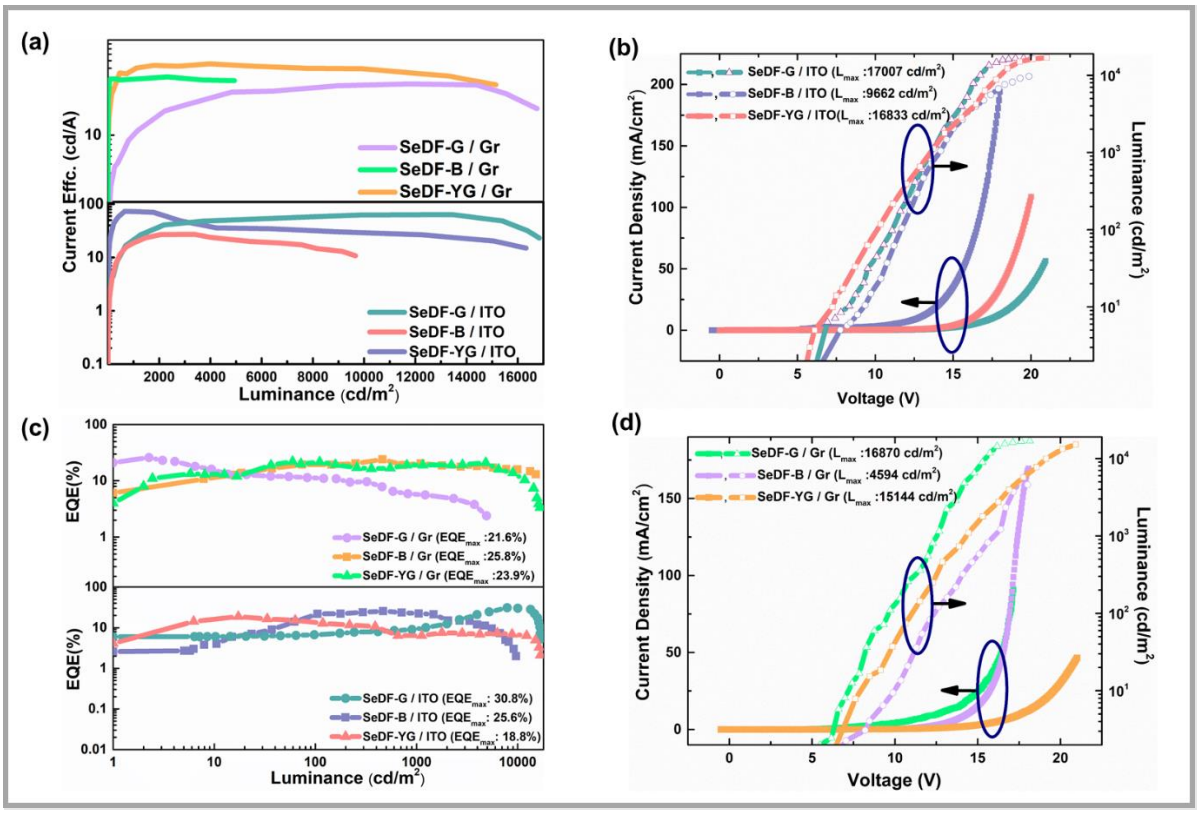

Figure 6. OLED characteristics, **a** Current Efficiency vs. Luminance of devices Gr-**SeDF-G**, Gr-**SeDF-B,** Gr-**SeDF-YG** and ITO-**SeDF-G**, ITO-**SeDF-B,** ITO-**SeDF-YG b**. Current density–voltage–luminance (J–V–L) characteristics of ITO-based OLEDs, **c**. EQE (%) vs. Luminance of devices Gr-**SeDF-G**, Gr-**SeDF-B,** Gr-**SeDF-YG** and ITO-**SeDF-G**, ITO-**SeDF-B,** ITO-**SeDF-YG, d.** Current density–voltage–luminance (J–V–L) characteristics of graphene-based OLEDs.

Once fully optimized, we prepared devices to compare the TADF materials both with Gr and ITO-based anodes. Six different device sets were fabricated using three different emitting dopants (**SeDF-G**, **SeDF-B,** and **SeDF-YG**) and two different anodes (graphene and ITO). m-CBP was chosen as a host material for all systems because of its high triplet energy of 2.9 eV, aligned HOMO and LUMO energy levels, a wide energy bandgap, and high morphological stability.[58]

Table 4. ((Summary of OLED characteristics of champion devices, (average inparenthesis).))

Device	Anode	Dopant	L_{MAX} ($cd.m^{-2}$)[a]	η_C ($cd.A^{-1}$)[b]	η_{EXT} (%)[c]	V_{on} (V)[d]	CIE (x, y)[e]
A	ITO	SeDF-G	17007 (16896)	64.0	30.8	4.3	(0.31,0.53)
B	Gr	SeDF-G	16870 (16290)	34.3	21.6	4.7	(0.36, 0.53)
C	ITO	SeDF-B	9662 (9641)	27.3	25.6	5.8	(0.17, 0.14)
D	Gr	SeDF-B	4594 (4508)	40.5	25.8	5.8	(0.19, 0.16)
E	ITO	SeDF-YG	16833 (16697)	73.5	18.8	5.4	(0.33, 0.48)
F	Gr	SeDF-YG	15144 (14222)	55.8	23.9	5.4	(0.37, 0.51)
Ref[[28]]	ITO	Px2BP*	86100	35.9	10.7	3.2	(0.37, 0.58)
Ref[[28]]	ITO	P-PxBBP**	57120	20.1	6.9	3.6	(0.49, 0.51)

[a])((Peak luminance)); [b])((Peak current efficiency)); [c])((Peak external quantum efficiency (%))); [d])((The operating voltage at a brightness of $1cd.m^{-2}$)); [e])((Commission International L'Eclairage coordinates at ~$1000cd.m^{-2}$));

* 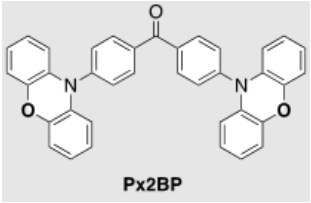

** 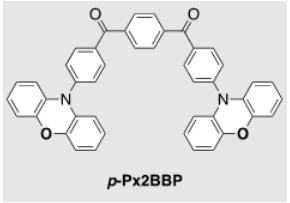

Figure. 6 illustrates the EQE-current efficiency vs. Voltage and I-V-J graphs for the fabricated devices, and Table 4 summarizes the key results. The amount of emitter dopant dispersed was 10% (v/v) to avoid exciton annihilation and high current density, and to give direct comparison to the photophysical results in the same host and doping ratio.[59] Photographs of the working devices are shown in Figure. 7a, and the color coordinates (x,y) are marked on the chromaticity diagram in Figure. 7b. There is a noticeable red shift for graphene-based OLEDs compared to ITO-based devices in their EL spectrum (Figure. 7c), demonstrating that the recombination zones of graphene-based devices are closer to the cathode, a highly desirable phenomenon for increased efficiency.[60]Among all device architectures, the highest EQE value was measured for **SeDF-G**-based OLEDs fabricated by using ITO as the anode (max EQE 30.8%), higher than its Gr counterpart (21.6%). This study reveals the effect of spin orbit coupling via the EQE values, because the maximum EQE values for sulfur substituted molecules could not exceed the 20% EQE. [32,33]This observation can be correlated to the lower current density values measured for the aforementioned device architecture as it operates. Furthermore, improved hole injection from anode to emissive layer in **SeDF-G** / ITO could be another reason, which can be explained by the lower turn-on voltage of **SeDF-G** / ITO.

Pleasingly, the blue device with the graphene anode (**SeDF-B** / Gr) exhibited a much higher current efficiency (40.5 cd/A) than that with the ITO anode (27.3 cd/A) and coherent blue electroluminescence spectra with a Commission Internationale de l'Eclairage (CIE) coordinates (0.19, 0.16). According to Figure. 6a and 4c, when **SeDF-B** is used as the emitting dopant, the EQE values in both Gr- and ITO-based OLEDs decrease rapidly after reaching high luminance values. This efficient roll-off at high current density is mainly attributed to excess T_1 excitons accumulating in the emitting layer, which cause exciton quenching by triplet-triplet and/or singlet-triplet annihilation.[61]

Additionally, a highly efficient flexible phosphorescent yellowish-green OLED was fabricated using Gr as the anode and **SeDF-YG** emitter. The device showed much higher EQE values (23.9%) than the ITO-based device (18.8%). ITO-**SeDF-YG** has a lower EQE, although it has higher current efficiency and almost the same luminance and turn-on voltage as Gr-**SeDF-YG**. Lower EQE value could be explained by the increased joule heating during operation in ITO-**SeDF-YG**, although it shows superior charge injection characteristics.[62]

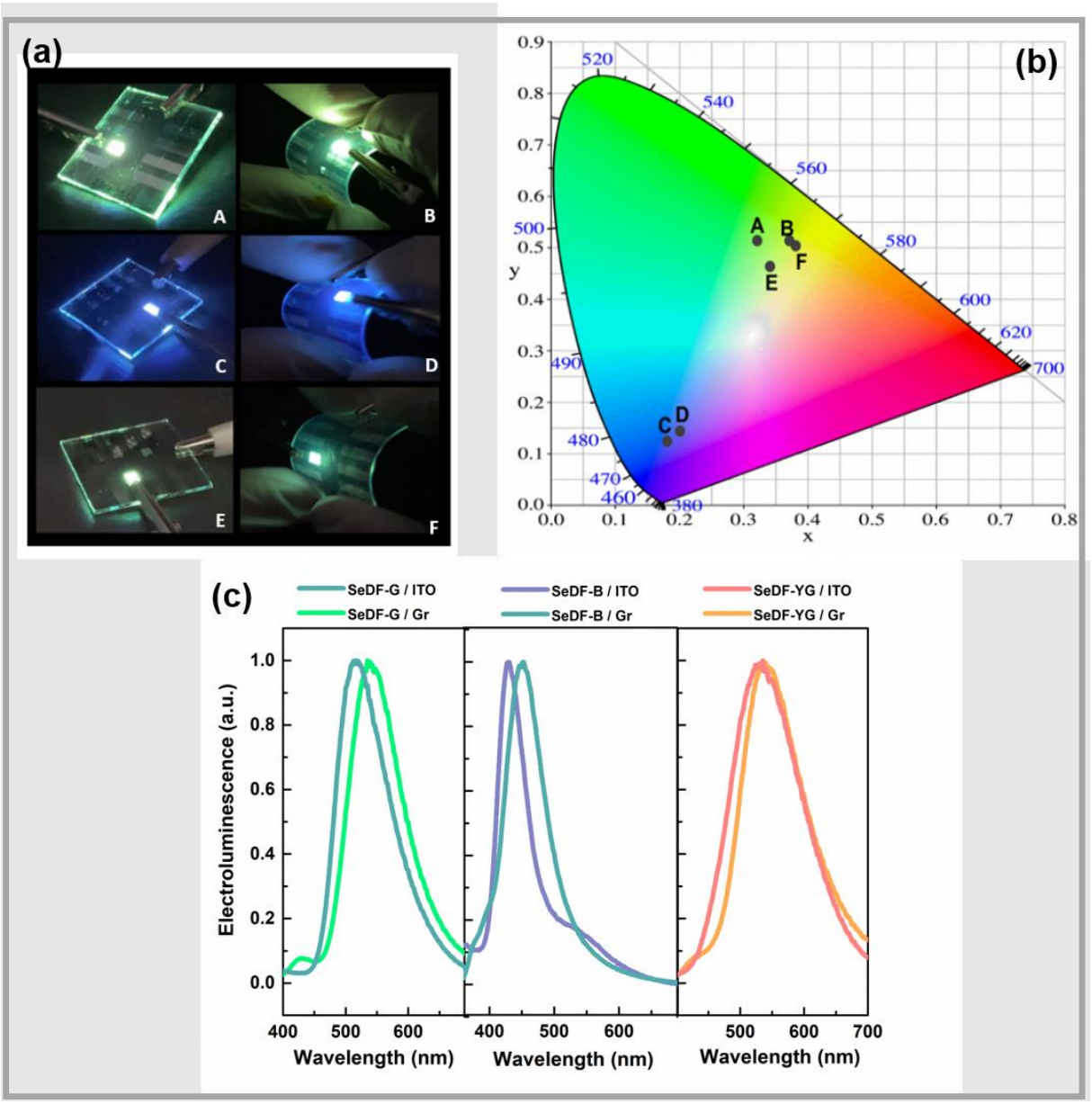

Figure 7. a) Photographs of ITO based and graphene-based OLED devices (A: **SeDF-G** / ITO, B: **SeDF-G** /Gr, C: **SeDF-B** / ITO, D: SeDF-B / Gr, E: SeDF-YG / ITO, F: SeDF-YG / Gr). b) Chromaticity diagram of OLED devices. c) Electroluminescence vs. wavelength graphs of

devices: (**SeDF-G** / ITO and **SeDF-G** / Gr), (**SeDF-B** / ITO and **SeDF-B** / Gr), (**SeDF-YG** / ITO and **SeDF-YG** / ITO).

The stability of all devices is evaluated with an initial luminance (L_0), 1000 cd m^{-2} to determine the operational lifetime (Supplementary Fig.S10). For ITO-based devices LT80 values were determined to be 283h for SeDF-G, 29h for SeDF-B and 289 for SeDF-YG where for graphene-based devices LT80s were recorded as 178h 10h 114h for SeDF-G, SeDF-B and SeDF-YG respectively. For green and yellow-green emitters LT80 values between 200-500 h were commonly demonstrated in literature which is consistent with our results. However much higher performances have also been realized (over 15000h) with lower operational L_0. For blue emitters stabilities are generally much lower with a commonly observed range between 20 to 100h. Even though significantly high device performance was observed with materials introduced in this work, stability of the devices could still be improved through interface engineering and our work along these lines are currently underway. One important point to note here is the fact that although high doped flexible graphene electrodes were utilized, the stabilities observed for these devices are quite compatible to ITO-based counterparts which is quite encouraging for utilization of these flexible devices in future relevant applications. [37,63–66]

To further support our device results, PLQYs of equivalent films (10% TADF emitter in m-CBP host, under nitrogen in integrating sphere with 330 nm excitation) were investigated. The measured values are surprisingly low considering the efficiency of the devices, at only 2.6%, 7.6%, and 8.5% for SeDF-B, SeDF-G, and SeDF-YG respectively (Table. S4). A strong correlation between PLQY and device EQE has been clearly demonstrated in the literature.[67] We believe the possible explanation is that the evaporation of the films causes a difference in the contribution of axial/equatorial conformers, with the more efficient and narrower conformer

dominating in the evaporated films. To the best of our knowledge this is the first example where a high energy conformer has been exclusively stabilized in evaporated films. This exclusivity is evident by considering that if a mixture of conformers were present, then FRET would quench all the high energy states.[68,69] We suggest that precisely this occurs in the drop-cast films and in solution, where the efficiency is lower, and the emission band is lower-energy and broader than the EL of the devices (Figure 3 and 7c). Further work to determine the conformer differences in the evaporated and drop-cast films is currently underway in our laboratories.

The results overall demonstrate that Gr/PET anodes are extremely promising candidates to replace ITO for next-generation flexible solid-state lighting device technologies. These Gr anodes are also fully compatible with TADF emissive layers, unlocking high efficiencies. Last but not least, EQEs observed from OLEDs utilizing **SeDF-G** and **SeDF-YG** (ITO/Glass) are almost three times higher than devices using their selenium free analogs (Px2BP and *p*-Px2BBP) with practically the same device structures (Table 2). This clearly demonstrates the success of the rational design approach introduced in this work, and the efficiency improvements that can be accessed using the heavy-atom effect to improve H_{SO}.

4. Conclusion

The efficacy of RISC in TADF systems is proportional to H_{SO} and inversely proportional to ΔE_{ST}. While different approaches have been pursued for minimizing ΔE_{ST} with transformative success, the effect is not as easy to investigate. Here, TADF materials with heavy-atom selenium incorporation (**SeDF-G**, **SeDF-B**, **SeDF-YG**) was designed and synthesized in this work. The materials showed remarkable performance where EQEs over 30% were achieved with **SeDF-G** higher than both oxygen and sulfur-based ones. OLEDs utilizing **SeDF-G** and **SeDF-YG** are almost three times higher than devices using their selenium-free phenoxazine analogs with practically the same device structures. Additionally, for the first-time flexible Gr-

based electrodes were developed for TADF OLEDs and revealed to match ITO/glass performance in many cases. Remarkably, Gr-based devices showed higher performance compared to their ITO analogs in pure blue OLED devices (EQEs, 25.6% vs. 25.8%).

5. Methods

Graphene Growth: A 25 µm-thick cold rolling copper was used as a growth substrate to achieve highly uniform large area graphene films. Another key step is the pre-cleaning of copper by using acid treatment. These steps significantly improve both uniformity and morphology by lifting the oxide layer and removing the existing impurities on the copper foil. For that purpose, acetic acid is used as a pre-cleaning treatment which follows standard cleaning steps. Then, a copper substrate is subjected to a significant Ar flow and annealed with H_2 at 1000 ºC to remove native oxides from the copper surface. The growth is performed by mixing gases of CH4: H2 (2:35 sccm) for 35 minutes. The SLG/copper sample is then rapidly cooled to room temperature under Ar gas flow. To form 7LG, the SLG/copper sample is stacked to PET using the lamination technique, then copper is etched using copper etchant ($Fecl_3$). This process is repeated 7 times to release 7LG. In last-layer doping, after last layer laminating, the sample is soaked in nitric acid for 5 minutes and then dried with nitrogen gun.

OLED Fabrication: The graphene on the pet substrate was first exposed to oxygen plasma for 5 minutes. The hole injection layer, which was made up of PEDOT:PSS and IPA in a 1:1.5 ratio, was spin-coated to create a 40-nm thick film on top of the anodes and then baked for 15 minutes in air at 80 degrees. The oxygen plasma time is 15 minutes for ITO-coated glasses. Organic layers are made up of α-NPD, which serves as an HTL, and TPBI, which works as ETL. The dopants SeDF-G, SeDF-B, and SeDF-YG are green, blue, and yellowish green, respectively, and were deposited on the emissive layer next to the host material m-CBP. In all devices, the host-to-dopant ratio is 90:10 (v/v). Lithium fluoride (LiF) (0.6 nm)/aluminum (Al)

(100 nm) cathode layers were deposited under a high vacuum. All thermal vapor depositions were performed at a pressure of less than 10^{-6} torr. The device area was around 4-6 mm^2. Green, blue, and yellowish-green OLEDs were successfully fabricated by using graphene and ITO anodes.

The device architecture of the former was PET/Graphene/HIL(40nm)/ α-NPD (40nm)/EML(20nm)/TPBI(80nm)/LiF(0.6nm)/Al(100nm). The latter's device architecture was Glass/ITO/ α-NPD (40nm)/EML(20nm)/TPBI(40nm)/LiF(0.6nm) /Al(100nm). All of the measurements were performed in a glove box.

Computational Methods: Density functional theory (DFT) methods were applied for TADF material candidates at the B3LYP hybrid functional and 6-311+G(d,p) basis set level using tight convergence criteria at 10^{-8} for RMS density matrix convergence and 10^{-6} for energy in the Gaussian09 (Revision A.02) software package. [70–73] Structures and vertical excitation energies were compared PBE0 functionals at lower and higher basis sets (Table S1). General trends among molecules are similar, and the basis set is adequate. Although B3LYP underestimates excited state energy levels, it predicts HOMO level better for this study and gives comparable results with PBE0 (Table S1). Geometry optimizations were initiated from different initial structures by controlling torsional angle between connected center, bridge, and side units of TADF candidates to achieve the lowest energy geometry. Electrostatic potential surface (ESP), highest occupied molecular orbitals (HOMO), and lowest unoccupied molecular orbitals (LUMO) were determined and mapped onto the two of the optimized lowest energy conformers, which are quasi-equatorial and quasi-axial conformations of selenium substitutes phenoxazine donor unit. The singlet and triplet excited states were calculated by using time-dependent density-functional theory (TDDFT) at the same calculation level quasi-equatorial conformation and quasi-axial conformations. Natural transition orbitals were determined for the transitions with high probabilities. [74] Vertical (VIP) and adiabatic ionization potential (AIP) were calculated by the energy difference between the neutral molecule and cation state of the ground

state and reoptimized geometry. Vertical Electron Affinity (VEA) was also calculated by considering the transition from the neutral ground state to the anion at the ground state. Hole reorganization energies (λ_{hole}) were determined based on the formulation by Bredas et al to determine structural response to the electronic alterations. [75] Charge transfer (δ) between donor and acceptor units were calculated by using the electrostatic potential charge fitting scheme. [76] Dipole moment (μ), isotropic polarizability (α), and the first order static hyperpolarizability (β) were calculated. Rate constant for the RISC between T_1 and S_1 excited state levels were calculated by using non-adiabatic expression similar with the Marcus Theory where λ_M is the Marcus reorganization energy of the molecule related with the inter- and intra-molecular low-frequency vibrations for the transition between different excited states predicted between 0.1-0.2 according the Bredas et al [75], H_{SO} is the spin orbit coupling matrix element calculated at the same quality by using ORCA 5.0 software.[77]

$$k_{rISC} = \frac{2\pi}{\hbar}|H_{SO}|^2(4\pi\lambda k_B T)^{-\frac{1}{2}}\exp(-\frac{(\Delta E_{ST} + \lambda)^2}{4\lambda k_B T})$$

Acknowledgements

((This study was supported by TUBITAK under project no. 115F604. Erol Yıldırım gratefully acknowledges support from 2232 International Fellowship for Outstanding Researchers Program of TUBITAK (Project No: 118C251). The authors thank Mustafa Yaşa for the help in the design of the figures.))

References

[1] R. H. Friend, R. W. Gymer, A. B. Holmes, J. H. Burroughes, R. N. Marks, C. Taliani, D. D. C. Bradley, D. A. Dos Santos, J. L. Brédas, M. Lögdlund, W. R. Salaneck, *Nature* **1999**, *397*, 121.

[2] C. Adachi, M. A. Baldo, M. E. Thompson, S. R. Forrest, *J. Appl. Phys.* **2001**, *90*, 5048.

[3] B. H. Wallikewitz, D. Kabra, S. Gélinas, R. H. Friend, *Phys. Rev. B - Condens. Matter Mater. Phys.* **2012**, *85*, 22.

[4] J. Xue, C. Li, L. Xin, L. Duan, J. Qiao, *Chem. Sci.* **2016**, *7*, 2888.

[5] D. de Sa Pereira, D. R. Lee, N. A. Kukhta, K. H. Lee, C. L. Kim, A. S. Batsanov, J. Y. Lee, A. P. Monkman, *J. Mater. Chem. C* **2019**, *7*, 10481.

[6] N. A. Kukhta, H. F. Higginbotham, T. Matulaitis, A. Danos, A. N. Bismillah, N. Haase, M. K. Etherington, D. S. Yufit, P. R. McGonigal, J. V. Gražulevičius, A. P. Monkman, *J. Mater. Chem. C* **2019**, *7*, 9184.

[7] B. H. Drummond, G. C. Hoover, A. J. Gillett, N. Aizawa, W. K. Myers, B. T. McAllister, S. T. E. Jones, Y.-J. Pu, D. Credgington, D. S. Seferos, *J. Phys. Chem. C* **2020**, *124*, 6364.

[8] T. Cardeynaels, S. Paredis, A. Danos, D. Vanderzande, A. P. Monkman, B. Champagne, W. Maes, *Dye. Pigment.* **2021**, *186*, 109022.

[9] S. Paredis, T. Cardeynaels, J. Deckers, A. Danos, D. Vanderzande, A. P. Monkman, B. Champagne, W. Maes, *J. Mater. Chem. C* **2022**, *10*, 4775.

[10] T. Cardeynaels, S. Paredis, A. Danos, A. Harrison, J. Deckers, S. Brebels, L. Lutsen, D. Vanderzande, A. P. Monkman, B. Champagne, W. Maes, *Dye. Pigment.* **2021**, *190*, 109301.

[11] J. S. Ward, A. Danos, P. Stachelek, M. A. Fox, A. S. Batsanov, A. P. Monkman, M. R. Bryce, *Mater. Chem. Front.* **2020**, *4*, 3602.

[12] G. Haykir, M. Aydemir, A. Tekin, E. Tekin, A. Danos, F. Yuksel, G. Hizal, A. P. Monkman, F. Turksoy, *Mater. Today Commun.* **2022**, *31*, 103550.

[13] A. Danos, D. Gudeika, N. A. Kukhta, R. Lygaitis, M. Colella, H. F. Higginbotham, A. N. Bismillah, P. R. McGonigal, J. V. Grazulevicius, A. P. Monkman, *J. Mater. Chem. C* **2022**, *10*, 4737.

[14] G. Haykir, M. Aydemir, A. Danos, S. Gumus, G. Hizal, A. P. Monkman, F. Turksoy, *Dye. Pigment.* **2021**, *194*, 109579.

[15] J. Zhu, D. Han, X. Wu, J. Ting, S. Du, A. C. Arias, *ACS Appl. Mater. Interfaces* **2020**, *12*, 31687.

[16] C. Keum, C. Murawski, E. Archer, S. Kwon, A. Mischok, M. C. Gather, *Nat. Commun.* **2020**, *11*, 6250.

[17] A. H. Castro Neto, F. Guinea, N. M. R. Peres, K. S. Novoselov, A. K. Geim, *Rev. Mod. Phys.* **2009**, *81*, 109.

[18] C. Soldano, A. Mahmood, E. Dujardin, *Carbon N. Y.* **2010**, *48*, 2127.

[19] A. K. Geim, *Science (80-.).* **2009**, *324*, 1530.

[20] T. H. Han, Y. Lee, M. R. Choi, S. H. Woo, S. H. Bae, B. H. Hong, J. H. Ahn, T. W. Lee, *Nat. Photonics* **2012**, *6*, 105.

[21] N. Li, S. Oida, G. S. Tulevski, S. J. Han, J. B. Hannon, D. K. Sadana, T. C. Chen, *Nat. Commun.* **2013**, *4*, 1.

[22] J. Meyer, P. R. Kidambi, B. C. Bayer, C. Weijtens, A. Kuhn, A. Centeno, A. Pesquera, A. Zurutuza, J. Robertson, S. Hofmann, *Sci. Rep.* **2014**, *4*, 1.

[23] T. H. Han, M. H. Park, S. J. Kwon, S. H. Bae, H. K. Seo, H. Cho, J. H. Ahn, T. W. Lee, *NPG Asia Mater.* **2016**, *8*, 1.

[24] J. Lee, T. H. Han, M. H. Park, D. Y. Jung, J. Seo, H. K. Seo, H. Cho, E. Kim, J. Chung, S. Y. Choi, T. S. Kim, T. W. Lee, S. Yoo, *Nat. Commun.* **2016**, *7*, 1.

[25] S. J. Kwon, T. H. Han, T. Y. Ko, N. Li, Y. Kim, D. J. Kim, S. H. Bae, Y. Yang, B. H. Hong, K. S. Kim, S. Ryu, T. W. Lee, *Nat. Commun.* **2018**, *9*, 1.

[26] A. Rodriguez-Serrano, V. Rai-Constapel, M. C. Daza, M. Doerr, C. M. Marian, *Phys. Chem. Chem. Phys.* **2015**, *17*, 11350.

[27] D. Y. Kondakov, J. R. Sandifer, C. W. Tang, R. H. Young, *J. Appl. Phys.* **2003**, *93*, 1108.

[28] S. Y. Lee, T. Yasuda, Y. S. Yang, Q. Zhang, C. Adachi, *Angew. Chemie - Int. Ed.* **2014**, *53*, 6402.

[29] G. C. Hoover, D. S. Seferos, *Chem. Sci.* **2019**, *10*, 9182.

[30] C. L. Kim, J. Jeong, D. R. Lee, H. J. Jang, S.-T. Kim, M.-H. Baik, J. Y. Lee, *J. Phys. Chem. Lett.* **2020**, *11*, 5591.

[31] Y. X. Hu, J. Miao, T. Hua, Z. Huang, Y. Qi, Y. Zou, **2022**, 1.

[32] I. Marghad, D. H. Kim, X. Tian, F. Mathevet, C. Gosmini, J.-C. Ribierre, C. Adachi, *ACS Omega* **2018**, *3*, 2254.

[33] S. Xiang, R. Guo, Z. Huang, X. Lv, S. Sun, H. Chen, Q. Zhang, L. Wang, *Dye. Pigment.* **2019**, *170*, 107636.

[34] H. Tanaka, K. Shizu, H. Nakanotani, C. Adachi, *J. Phys. Chem. C* **2014**, *118*, 15985.

[35] K. Wang, Y.-Z. Shi, C.-J. Zheng, W. Liu, K. Liang, X. Li, M. Zhang, H. Lin, S.-L. Tao, C.-S. Lee, X.-M. Ou, X.-H. Zhang, *ACS Appl. Mater. Interfaces* **2018**, *10*, 31515.

[36] S. Xiang, R. Guo, Z. Huang, X. Lv, S. Sun, H. Chen, Q. Zhang, L. Wang, *Dye. Pigment.* **2019**, *170*, 107636.

[37] M. Okazaki, Y. Takeda, P. Data, P. Pander, H. Higginbotham, A. P. Monkman, S. Minakata, *Chem. Sci.* **2017**, *8*, 2677.

[38] D. R. Lee, K. H. Lee, W. Shao, C. L. Kim, J. Kim, J. Y. Lee, *Chem. Mater.* **2020**, *32*, 2583.

[39] N. A. Kukhta, M. R. Bryce, *Mater. Horizons* **2021**, *8*, 33.

[40] G. Tin, T. Mohamed, N. Gondora, M. A. Beazely, P. P. N. Rao, *Medchemcomm* **2015**, *6*, 1930.

[41] E. Aksoy, A. Danos, C. Li, A. P. Monkman, C. Varlikli, *J. Phys. Chem. C* **2021**, *125*, 13041.

[42] N. Haase, A. Danos, C. Pflumm, A. Morherr, P. Stachelek, A. Mekic, W. Brütting, A. P. Monkman, *J. Phys. Chem. C* **2018**, *122*, 29173.

[43] M. Hempe, N. A. Kukhta, A. Danos, M. A. Fox, A. S. Batsanov, A. P. Monkman, M. R. Bryce, *Chem. Mater.* **2021**, *33*, 3066.

[44] S. Sem, S. Jenatsch, K. Stavrou, A. Danos, A. P. Monkman, B. Ruhstaller, *J. Mater. Chem. C* **2022**, *10*, 4878.

[45] S. Bae, H. Kim, Y. Lee, X. Xu, J. S. Park, Y. Zheng, J. Balakrishnan, T. Lei, H. Ri Kim, Y. Il Song, Y. J. Kim, K. S. Kim, B. Özyilmaz, J. H. Ahn, B. H. Hong, S. Iijima, *Nat. Nanotechnol.* **2010**, *5*, 574.

[46] X. Li, C. W. Magnuson, A. Venugopal, J. An, J. W. Suk, B. Han, M. Borysiak, W. Cai, A. Velamakanni, Y. Zhu, L. Fu, E. M. Vogel, E. Voelkl, L. Colombo, R. S. Ruoff, *Nano Lett.* **2010**, *10*, 4328.

[47] Y. Zhang, L. Zhang, P. Kim, M. Ge, Z. Li, C. Zhou, *Nano Lett.* **2012**, *12*, 2810.

[48] I. Vlassiouk, M. Regmi, P. Fulvio, S. Dai, P. Datskos, G. Eres, S. Smirnov, *ACS Nano* **2011**, *5*, 6069.

[49] D. Senyildiz, O. T. Ogurtani, G. Cambaz Buke, *Appl. Surf. Sci.* **2017**, *425*, 873.

[50] A. C. Ferrari, J. C. Meyer, V. Scardaci, C. Casiraghi, M. Lazzeri, F. Mauri, S. Piscanec, D. Jiang, K. S. Novoselov, S. Roth, A. K. Geim, *Phys. Rev. Lett.* **2006**, *97*, 187401.

[51] A. Kasry, M. A. Kuroda, G. J. Martyna, G. S. Tulevski, A. A. Bol, *ACS Nano* **2010**, *4*, 3839.

[52] Z. Wenjin, B. Ran, Z. Hongmei, H. Wei, *J. Appl. Phys.* **2014**, *116*, 224502.

[53] W. Zhang, X. Bi, X. Zhao, Z. Zhao, J. Zhu, S. Dai, Y. Lu, S. Yang, *Org. Electron.* **2014**, *15*, 3445.

[54] W. H. Lee, D. H. Kim, P. Justin Jesuraj, H. Hafeez, J. C. Lee, D. K. Choi, T.-S. Bae, S. M. Yu, M. Song, C. S. Kim, S. Y. Ryu, *Mater. Res. Express* **2018**, *5*, 076201.

[55] X. F. Peng, X. Y. Wu, X. X. Ji, J. Ren, Q. Wang, G. Q. Li, X. H. Yang, *J. Phys. Chem. Lett.* **2017**, *8*, 4691.

[56] S. H. Chen, *J. Appl. Phys.* **2005**, *97*.

[57] J. Xin, P. Sun, F. Zhu, Y. Wang, D. Yan, *J. Mater. Chem. C* **2021**, *9*, 2236.

[58] T. Furukawa, H. Nakanotani, M. Inoue, C. Adachi, **2015**, 1.

[59] S. J. Yoon, H. J. Lee, K. H. Lee, J. Y. Lee, *J. Mater. Chem. C* **2020**, *8*, 7485.

[60] P. J. Jesuraj, H. Hafeez, D. H. Kim, J. C. Lee, W. H. Lee, D. K. Choi, C. H. Kim, M. Song, C. S. Kim, S. Y. Ryu, *J. Phys. Chem. C* **2018**, *122*, 2951.

[61] Y. Zhang, S. R. Forrest, *Phys. Rev. Lett.* **2012**, *108*, 1.

[62] A. Kirch, A. Fischer, M. Liero, J. Fuhrmann, A. Glitzky, S. Reineke, *Light Sci. Appl.* **2020**, *9*.

[63] Advanced Materials - 2015 - Kim - Highly Efficient Simplified Solution-Processed Thermally Activated Delayed-Fluorescence.pdf, .

[64] 10. Advanced Optical Materials - 2021 - Chen - Highly Efficient and Solution-Processed Single-Emissive-Layer Hybrid White.pdf, .

[65] Angewandte Chemie - 2022 - Tang - Highly Robust CuI-TADF Emitters for Vacuum-Deposited OLEDs with Luminance up to 222 200.pdf, .

[66] L. S. Cui, A. J. Gillett, S. F. Zhang, H. Ye, Y. Liu, X. K. Chen, Z. Sen Lin, E. W. Evans, W. K. Myers, T. K. Ronson, H. Nakanotani, S. Reineke, J. L. Bredas, C. Adachi, R. H. Friend, *Nat. Photonics* **2020**, *14*, 636.

[67] H. Shi, W. Jing, W. Liu, Y. Li, Z. Li, B. Qiao, S. Zhao, Z. Xu, D. Song, *ACS Omega* **2022**, *7*, 7893.

[68] R. S. Nobuyasu, J. S. Ward, J. Gibson, B. A. Laidlaw, Z. Ren, P. Data, A. S. Batsanov, T. J. Penfold, M. R. Bryce, F. B. Dias, *J. Mater. Chem. C* **2019**, *7*, 6672.

[69] M. K. Etherington, F. Franchello, J. Gibson, T. Northey, J. Santos, J. S. Ward, H. F. Higginbotham, P. Data, A. Kurowska, P. L. Dos Santos, D. R. Graves, A. S. Batsanov, F. B. DIas, M. R. Bryce, T. J. Penfold, A. P. Monkman, *Nat. Commun.* **2017**, *8*, 1.

[70] P. J. Stephens, F. J. Devlin, C. F. Chabalowski, M. J. Frisch, *J. Phys. Chem.* **1994**, *98*, 11623.

[71] A. D. Becke, *J. Chem. Phys.* **1993**, *98*, 5648.

[72] C. Lee, W. Yang, R. G. Parr, *Phys. Rev. B* **1988**, *37*, 785.

[73] J. V. O. and D. M. J. Frisch, G. W. Trucks, H. B. Schlegel, G. E. Scuseria, M. A. Robb, J. R. Cheeseman, G. Scalmani, V. Barone, G. A. Petersson, H. Nakatsuji, X. Li, M. Caricato, A. Marenich, J. Bloino, B. G. Janesko, R. Gomperts, B. Mennucci, H. P. Hratchian, .

[74] R. L. Martin, *J. Chem. Phys.* **2003**, *118*, 4775.

[75] P. K. Samanta, D. Kim, V. Coropceanu, J.-L. Brédas, *J. Am. Chem. Soc.* **2017**, *139*, 4042.

[76] B. H. Besler, K. M. Merz, P. A. Kollman, *J. Comput. Chem.* **1990**, *11*, 431.

[77] F. Neese, *Wiley Interdiscip. Rev. Comput. Mol. Sci.* **2022**, 1.

The work here describes a new design principle for TADF-OLED materials, utilization of heavy atom selenium in donor segments, which results in enhanced reverse intersystem crossing and significant EQEs. First ever utilization of graphene electrodes in flexible OLEDs with TADF-based emitting layers and pure blue emitting devices with EQEs over 25% were also highlighted.

Parisa Sharif[‡], Eda Alemdar[‡], Soner Ozturk, Omer Caylan, Tugba Haciefendioglu, Goknur Buke,Murat Aydemir, Andrew Danos, Andrew P. Monkman, Erol Yildirim, Gorkem Gunbas, Ali Cirpan* Ahmet Oral**

Rational Molecular Design Enables Efficient Blue TADF–OLEDs with Flexible Graphene Substrate